



TECHNICAL ARTICLE

# Microstructure and Mechanical Properties of Electron Beam Welded Joints of Ti<sub>2</sub>AlNb Alloy

Zhiqiang Bu, Jiayun Wu, Xiuping Ma, Zeguo Li, and Jinfu Li

Submitted: 30 April 2022 / Revised: 24 August 2022 / Accepted: 17 September 2022 / Published online: 10 October 2022

A Ti<sub>2</sub>AlNb alloy was electron beam welded, and the microstructure and mechanical behavior of the welded joints were systematically investigated. In the as-welded joint, the fusion zone (FZ) is composed of single B2/ $\beta$  phase, while the heat-affected zone (HAZ) can be divided into two parts: HAZ I of B2/ $\beta$  and  $\alpha_2$  phases near the fusion line and HAZ II of B2/ $\beta$ ,  $\alpha_2$  and O phases near the base material. The as-welded joint exhibits a similar elongation to the base material at room temperature, but fractures without obvious plasticity at 650 °C. Annealing the welded joint at 810 °C for 2 h results in precipitation of lots of fine O phase from the B2/ $\beta$  matrix, due to which the mechanical performance of the welded joint is greatly improved, i.e., the elevated temperature elongation is increased to 7.3%, bringing about a synchronous rise in ultimate strength. Subjected to tensile test at room temperature, the as-welded joint generally fails along the fusion line while the as-annealed joint fails within the base material. In contrast, the fracture at elevated temperature constantly takes place in the FZ for all the joints. It is proved that electron beam welding and subsequent annealing is a promising way to link the Ti<sub>2</sub>AlNb alloy.

**Keywords** electron beam welding, mechanical properties, microstructure, Ti<sub>2</sub>AlNb alloy

## 1. Introduction

Ti<sub>2</sub>AlNb phase with ordered orthorhombic crystal structure was first discovered by Banerjee et al. (1988) in Ti-25Al-12.5Nb (at.%) alloy and the alloys based on Ti<sub>2</sub>AlNb phase in equilibrium are named Ti<sub>2</sub>AlNb-based alloys or directly Ti<sub>2</sub>AlNb alloys (Ref 1). With better high-temperature strength and oxidation resistance than conventional titanium alloys, Ti<sub>2</sub>AlNb alloys have been attracting much attentions as potential structural materials used at the temperatures ranging from 650 to 750 °C (Ref 2-6). Besides Ti<sub>2</sub>AlNb phase that is also called O phase, an actual Ti<sub>2</sub>AlNb alloy might also contain B2/ $\beta$  and  $\alpha_2$  phases, depending on the chemical composition and thermal-mechanical processing conditions, due to which the mechanical properties of Ti<sub>2</sub>AlNb alloys vary in a wide range.

The microstructure of Ti<sub>2</sub>AlNb alloys can be of fully lamellar structure, bimodal lamellar structure, Widmanstätten structure, equiaxed and duplex-type structure according to the morphologies of  $\alpha_2$  and O phases (Ref 7-9). In the relationship between microstructure and mechanical properties, B2/ $\beta$  phase is the major contributor to the ductility of the alloy; the granular  $\alpha_2$  phase can increase the strength of the alloy by inhibiting the

growth of B2/ $\beta$  phase and correspondingly refining the O phase; the lamellar O phase is favorable for strength, while the equiaxed O phase is advantageous to ductility. The Ti<sub>2</sub>AlNb alloy with the bimodal lamellar O phase structure has the best combination of ductility and strength, and its practical application has been put on the agenda (Ref 10-12). Consequently, the processing technologies including the welding of Ti<sub>2</sub>AlNb alloys should be considered.

There have been some reports on welding Ti<sub>2</sub>AlNb alloys, including diffusion bonding, TIG (tungsten inert gas) welding, friction welding and laser welding, etc. To promote element diffusion, a sufficiently high temperature has to be maintained in a diffusion bonding process due to the high melting point of Ti<sub>2</sub>AlNb alloy. This inevitably degrades the mechanical properties of the base material significantly (Ref 13, 14). Diffusion bonding is therefore infeasible for linking Ti<sub>2</sub>AlNb alloys. Shao et al. (Ref 15) explored the TIG welding of Ti<sub>2</sub>AlNb alloys. It was shown that the fusion zone, composed of  $\alpha_2 + \beta$ /B2 two phases, was much wider than in other fusion welding such as laser or electron beam welding, and the tensile mechanical properties of the joints were greatly deteriorated. Chen et al. (Ref 16, 17) studied the microstructure and mechanical properties of the linear friction welded Ti<sub>2</sub>AlNb alloy, and the weld zone was found to be mainly composed of LAGBs (low angle grain boundaries) due to insufficient dynamic recrystallization. The joint was basically comparable to the base metal in tensile strength at room temperature. However, limited by the technological characteristics, friction welding has high requirements on the shape and size of the workpiece. For example, it cannot be used for thin sheet workpiece. Laser welding shows great potential in welding the Ti<sub>2</sub>AlNb alloy, where the fusion zone is composed of single B2 phase due to the fast cooling rate, and the welded joint exhibits excellent tensile properties at room temperature (Ref 18, 19). However, the joint becomes brittle at 650 °C, due to the B2  $\rightarrow$  O phase transformation at the grain boundaries at 650 °C (Ref 20). Zhang et al. (Ref 21)

**Zhiqiang Bu** and **Jinfu Li**, State Key Laboratory of Metal Matrix Composites, School of Materials Science and Engineering, Shanghai Jiao Tong University, Shanghai 200240, People's Republic of China; and **Jiayun Wu**, **Xiuping Ma**, and **Zeguo Li**, AECC South Industry Company Limited, Zhuzhou 412002 Hunan, People's Republic of China. Contact e-mail: jfli@sjtu.edu.cn.

found that addition of TiB<sub>2</sub> powders during the laser welding could significantly depress the high-temperature brittleness of the welded joints.

Comparing to laser welding, electron beam welding has higher energy density, higher welding speed and smaller welding deformation. Thus, the electron beam welding can produce a weld with narrow and deep penetration, small heat-affected zone, and low residual stress (Ref 22-24). Electron beam welding may be more advantageous to weld Ti<sub>2</sub>AlNb alloy. However, there have been rare systematical reports on the electron beam welding of Ti<sub>2</sub>AlNb alloys to date, and the knowledge of the welding microstructure and its evolution during the post-weld annealing is inadequate. In this study, a Ti<sub>2</sub>AlNb alloy was joined by electron beam welding, and the microstructure and mechanical properties of the as-welded and as-annealed samples were systematically investigated.

## 2. Experimental Procedure

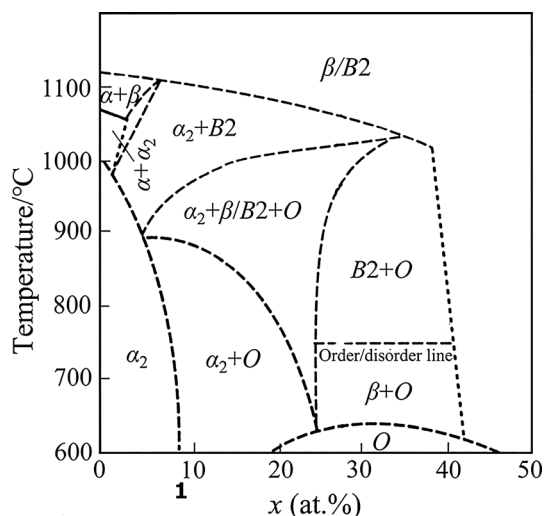
The Ti<sub>2</sub>AlNb alloy with a nominal composition of Ti-22Al-23Nb-1Mo-1Zr (at.%) was used for the welding experiments. Table 1 shows the actual chemical composition of the alloy measured by an inductively coupled plasma emission spectrometer (ICP).

Figure 1 shows the Ti-22Al-xNb phase diagram (Ref 25). The base material was isothermally forged at ~ 980 °C, solid solution treated at 960 °C for 1.5 h and then aged at 810 °C for 24 h. When the aging temperature was lower than 810 °C, the precipitates of O phase was so fine that the elongation was deteriorated. Aged at temperature higher than 810 °C, the strength would be decreased. Figure 2 shows the microstructure of the base alloy prior to welding. It consists of B2/ $\beta$  matrix with an average grain size of about 200  $\mu$ m, granular  $\alpha_2$  phase of about 2-3  $\mu$ m diameter and O phase. The distribution of  $\alpha_2$  phase is inhomogeneous, as shown in Fig. 2(a). Under the SEM, B2/ $\beta$  phase is bright,  $\alpha_2$  phase is dark and O phase has an intermediate contrast as shown in Fig. 2(b). The O phase varies greatly from one grain to another in morphology. The crystals formed during the solution treatment are thick lath shaped with a length of 3-8  $\mu$ m, while those formed during the aging treatment are fine and acicular with a length of 0.3-0.6  $\mu$ m.

The electron beam welding was performed using a THDW-15C type high voltage electron beam welding machine. During the welding, the electron beam spot was focused on the sample surface, the focusing current was 1800 mA, the acceleration voltage was 120 kV, the electron beam current was 12 mA, the welding speed was 1200 mm/min, and the pressure of the welding chamber was 0.4 Pa. Figure 3(a) shows the schematic of an as-welded sample. The thickness of the sample was 3 mm. There was no weld defect to be detected in the welded joint by x-ray penetration detection. After welding, some of the samples were annealed at 810 °C for 2 h and air cooled (810 °C/2 h/AC).

**Table 1 Chemical composition of the Ti<sub>2</sub>AlNb alloy used in the present work**

Elements	Al	Nb	Zr	Mo	Ti
Content (wt.%)	10.64	39.32	1.8	1.72	Bal



**Fig. 1** Phase diagram of Ti-22Al-xNb alloys

The metallographic specimens of the welded joints were prepared following conventional metallographic procedures. The specimens for electron backscattered diffraction (EBSD) analysis were prepared by electrochemically polishing with a solution of 6% perchloric acid, 34% butanol and 60% carbinol at the room temperature. The polishing voltage, current and time were 30 V, 0.6 A and 50 s, respectively. The microstructure was observed by an optical microscope (Leica DM 2700 M) and a scanning electron microscope (Tescan-Mira3). The element distribution in the joint was measured by energy disperse spectroscopy (EDS). The phase constitution in the welded joint was determined by an x-ray diffractometer (XRD Rigaku Smart Lab) with Cu K $\alpha$  radiation. The scan angle was between 20 and 90° with a speed of 4°/min. The microhardness was measured in a Vickers hardness tester (HVS-1000A) with a load of 200 g and a dwell time of 15 s. Taking the center of the fusion zone (FZ) as the original point, 13 points were measured on the both sides in the hardness test and the distance between two adjacent points was 150  $\mu$ m. The geometry of the tensile specimen is depicted in Fig. 2(b). The tensile tests at room temperature and 650 °C were performed on a universal material testing machine (Zwick/Roll Z100) with a strain rate of  $1.0 \times 10^{-3} \text{ s}^{-1}$ .

## 3. Results and Discussion

### 3.1 Microstructure

The microstructure of an electron beam welded joint is shown in Fig. 4. The welded joint consists of a fusion zone (FZ) and two heat-affected zones (HAZs). According to the thermal experience in the welding process and the microstructure, the HAZ can be further divided into HAZ I near the FZ and HAZ II near the base material (BM). As shown in Fig. 4(a), the width of the FZ, HAZ I and HAZ II is approximately 1200, 600 and 300  $\mu$ m, respectively. The FZ presents with a typical solidification structure, i.e., dendrites grow from the unmelted base material and are symmetrically distributed on both sides of the centerline of the FZ. There is no precipitated phase in the FZ, a little granular  $\alpha_2$  phase in HAZ I, but a large amount of lath O phase plus the  $\alpha_2$  phase in HAZ II.

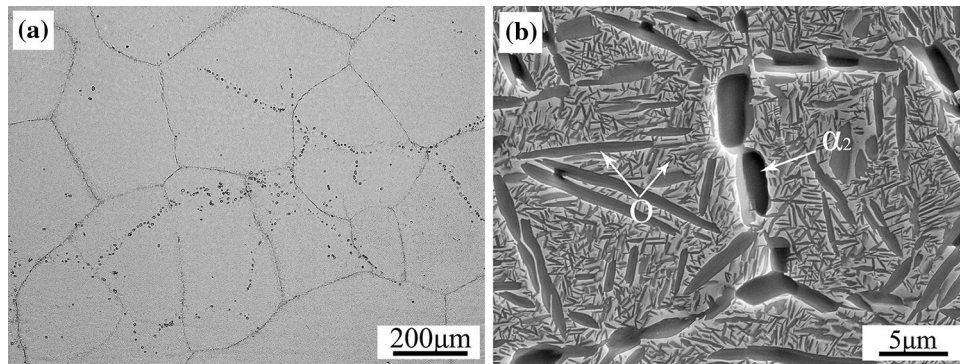


**Fig. 2** Microstructure of the base alloy: (a) low magnification OM image, (b) high magnification SEM image

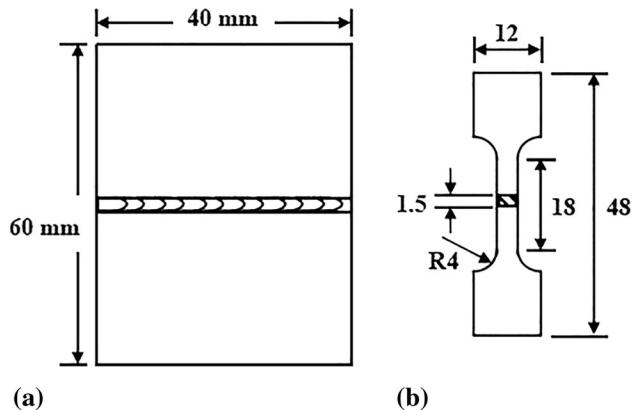


**Fig. 3** Schematic of the welded sample: (a) overall view, (b) geometry of the tensile specimen for mechanical property test

In a welding process, the material at different distances from the welding heat source experiences different thermal history, resulting in varying microstructures (Ref 18). The material in the FZ was fully melted and subsequently rapidly solidified into non-equilibrium microstructure because the latent heat of crystallization could be quickly dissipated through the unmelted solid. The critical cooling rates for the complete depression of  $\alpha_2$  and O phase precipitation from B2/ $\beta$  phase in Ti<sub>2</sub>AlNb alloy is 4 °C/s (Ref 26). As the cooling rate of the FZ was far larger than this critical value, there is only B2/ $\beta$  phase in the microstructure. For the material in HAZ I, it was heated at least into the B2 +  $\alpha_2$  two phase region and the O phase was completely decomposed.  $\alpha_2$  phase is high-temperature stable so that part of it could survive from the very fast heating and cooling cycle even if the temperature had been higher than the B2/ $\alpha_2$  phase transformation temperature during the welding. HAZ II is near to the base metal and the rise of temperature in it was relatively low during the welding. Thus, only the fine acicular O phase could be decomposed while the thick lath O phase, instead, grew into coarser plates, as shown in Fig. 4(d).

Figure 5 shows the EBSD images of a side of the as-welded joint. The FZ are mainly composed of columnar grains, reflecting the epitaxial growth of crystals from the base material. There are some fine equiaxed grains near the fusion line. The phase distribution mapping indicates that there is only single B2/ $\beta$  phase in the FZ (Fig. 5b), meaning that the cooling rate after solidification was larger than the critical cooling rates for both  $\alpha_2$  and O phases to be able to precipitate from the B2/ $\beta$  matrix. Indeed, the cooling rate in the FZ in an electric beam

welding process can reach hundreds of degrees per second. The feature of only B2/ $\beta$  phase in the FZ is also supported by the XRD pattern shown in Fig. 6.

Figure 7 shows the microstructure of the welded joint after annealed at 810 °C for 2 h and then cooled in air to room temperature (810 °C/2 h/AC). The annealing resulted in obvious changes in microstructure. The XRD patterns of the FZ shown in Fig. 6 clearly indicates that the diffraction peaks of B2 phase is significantly weakened after the annealing treatment, accompanied with the appearance of many peaks of O phase. Figure 7(b) shows that the FZ consists of lamellar O phase embedded in B2/ $\beta$  matrix. Besides the residual  $\alpha_2$  phase, there is very fine O phase present in HAZ I (Fig. 7c). Fine as well as coarse O phase are distributed in the B2/ $\beta$  matrix in HAZ II (Fig. 7d). However, the microstructure of the BM is basically unchanged. Figure 8 shows the EBSD analysis results of the annealed joint. The morphology of B2/ $\beta$  grains in the joint did not change due to the annealing except for the precipitation of O phase.

The B2/ $\beta$  phase in the FZ and HAZ of the as-welded joint formed in rapid cooling and is unstable in thermodynamics. It surely tends to decompose when the joint is annealed in the B2/ $\beta$  + O phase region, for example at 810 °C as done in the present work. It is argued that when a Ti<sub>2</sub>AlNb alloy is solid solution treated in the B2/ $\beta$  phase region and then furnace cooled to room temperature or aged in the B2/ $\beta$  + O phase region, lamellar O phase will be obtained (Ref 5, 8, 25). Generally, O phase first precipitated at the grain boundary of B2/ $\beta$  phase and developed into lamellar morphology toward the center of the B2/ $\beta$  grains in the FZ. In the different areas of HAZ, the original O phase was completely or partly decomposed during the welding. But it is believed that severe concentration fluctuation existed in the decomposed regions as the heating time was very short and the solute diffusion was inadequate, which in turn provided a large number of nucleation sites for the precipitation of O phase during the annealing. So, a high density of O phase precipitated from the B2/ $\beta$  mother phase in the HAZ during the annealing.

Figure 9 shows the element distribution in the welded joints. Obviously, there is no detectable element loss due to the welding since the content of each element across the FZ and BM is nearly the same. In Ti<sub>2</sub>AlNb alloys, B2/ $\beta$  phase is poor in Al but rich in Nb, and the reverse is the true for  $\alpha_2$  phase. In this sense, significant fluctuations should be observed on the EDS line scanning curve. On the other hand, the phases in the sample may be comparable to or even smaller than the incident electron beam diameter, due to which the difference of

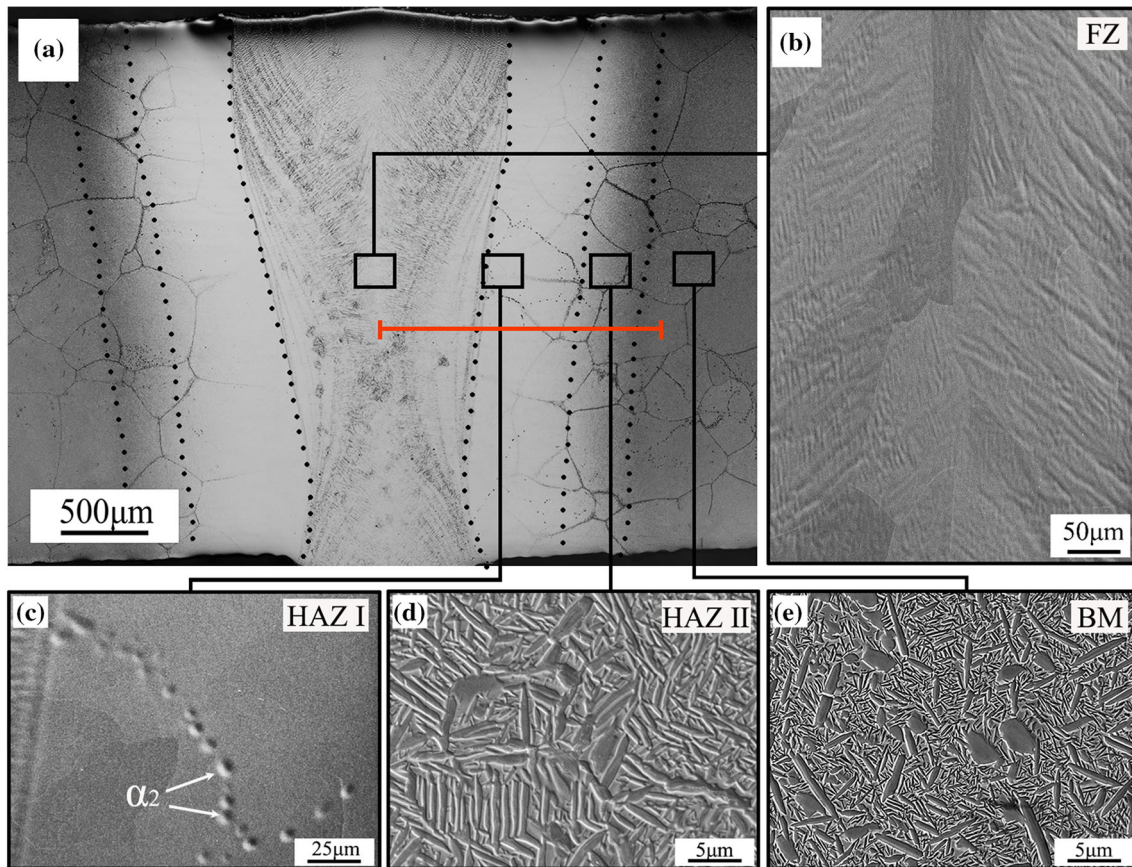


**Fig. 4** Microstructure of an as-welded joint: (a) overall view, (b) fusion zone (FZ), (c) HAZ near the FZ (HAZ I), (d) HAZ near the base material (HAZ II), (e) base materials. The red solid line denotes the path for EDS line scanning (Color figure online)

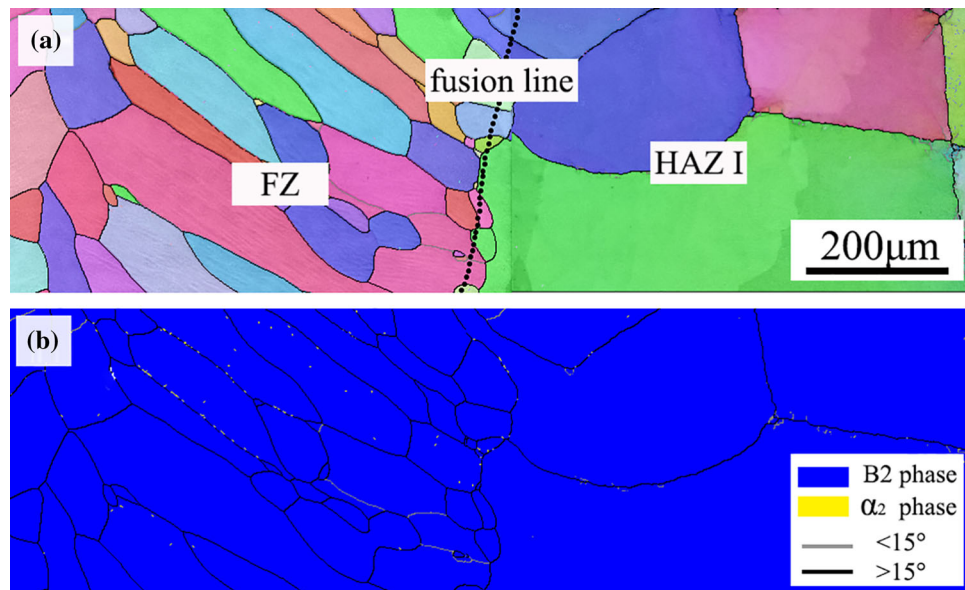


**Fig. 5** EBSD observation of an as-welded joint: (a) inverse pole figure and (b) phase mapping

concentration between different phases cannot fully be reflected on the scanning curve. The FZ is composed of single B2/ $\beta$  phase in the as welded state. Theoretically, the element distribution curve should be smooth if only taking the effect of phases into account. In contrary, the actual curve exhibits a relatively large fluctuation. Note that the dendrite arm spacing

in the solidification structure is far larger than the characteristic length of the solid phase transformed products such as O and  $\alpha_2$  phases (Fig. 4b) because the solute diffusion coefficient in liquid is generally 3 orders of magnitude larger than that in solid. The element distribution curve still presents a large fluctuation in the annealed FZ, and a very possible explanation

is that the solute concentration fluctuation resulted from the solidification segregation that could not be eliminated during the annealing at 810 °C for 2 h. The O phase precipitated from the HAZ in the annealing is so fine that the measured solute distribution curve was not influenced by it.

### 3.2 Microhardness

Microhardness distributions across the as-welded and 810 °C/2 h/AC annealed joints are shown in Fig. 10. In the

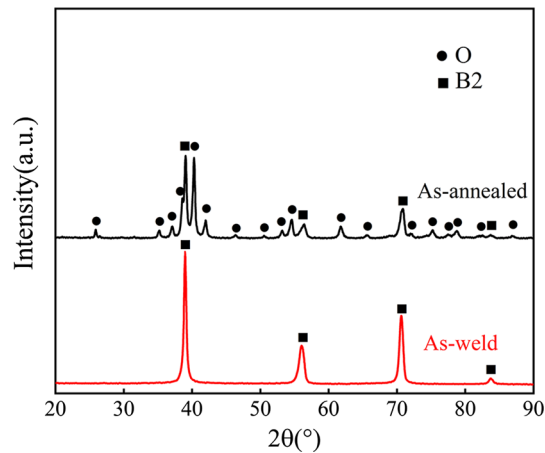


Fig. 6 XRD patterns of the fusion zone

as-welded joint, the boundary of FZ/HAZ exhibits the highest hardness and the hardness quickly decreases as the distance from the boundary increases. The lowest hardness occurs in the BM.

The microhardness of an alloy is mainly related to the quantity and size of the precipitates besides the matrix phase. The microhardness of HAZ II should be lower than that of the BM for a large mass of coarse O in HAZ II. However, the actual result is opposite. Some nanoscale O phase might be generated during the thermal cycle in the HAZ, which provides the HAZ with a higher microhardness. Further research is needed to explain this phenomenon. The FZ and HAZ I are mainly composed of B2/β phase. The finest B2/β grains in the FZ forms near the fusion line, as shown in Fig. 5(a), thus making the boundary of FZ/HAZ hardest. The strength of B2 phase is higher than O phase. The material can be strengthened only when the size and quantity of O phase are proper. Large O phase is disadvantageous for hardness.

The post-weld annealing resulted in a significant rise of microhardness in the welded joint (Fig. 10). The increment is around 50 HV or 15% in the FZ. Comparing Fig. 4 and 7, it is known that the increase of microhardness is related with the precipitation of fine O phase. The more and the smaller the precipitates, the higher the microhardness. As shown in Fig. 7, both HAZ I and FZ have a large amount of O phase. However, the O phase in HAZ I is smaller than in FZ, so the HAZ I is harder than FZ. The HAZ experienced a rapid thermal cycle during welding. In the heating the original O phase in HAZ I was completely dissolved but the solute elements did not have

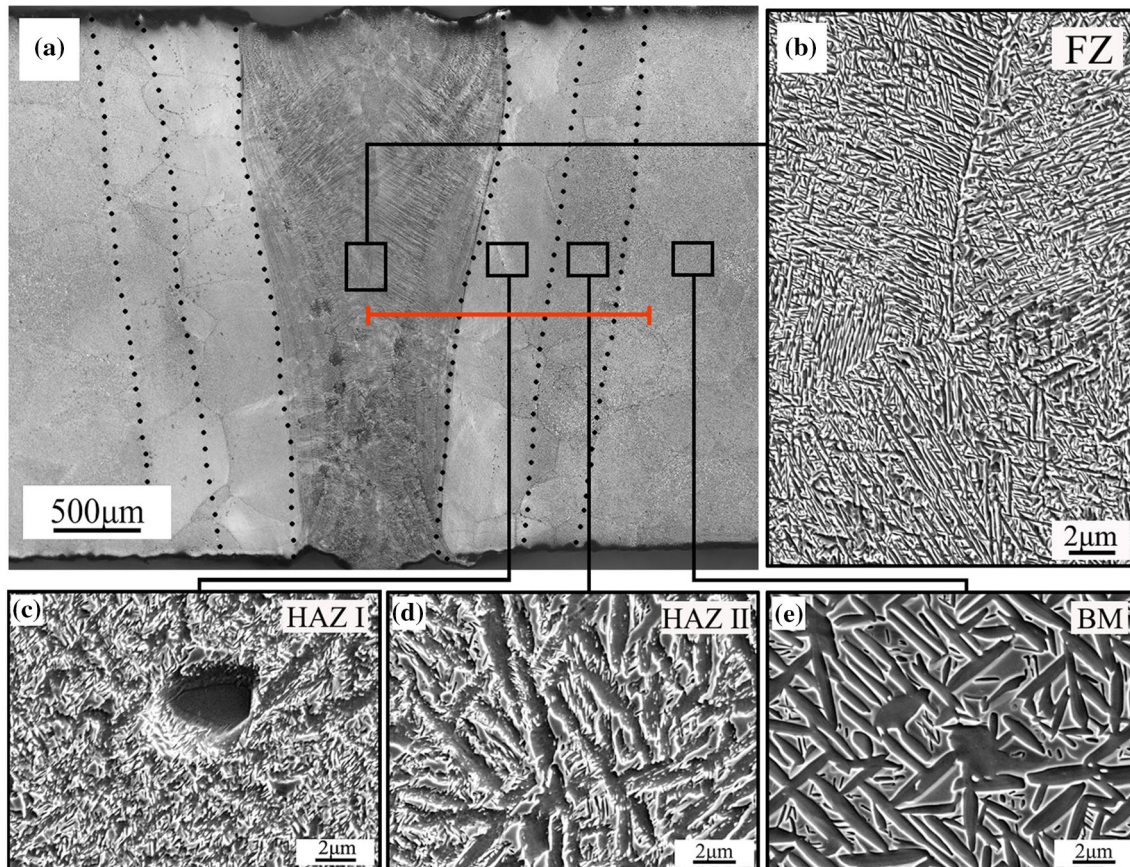
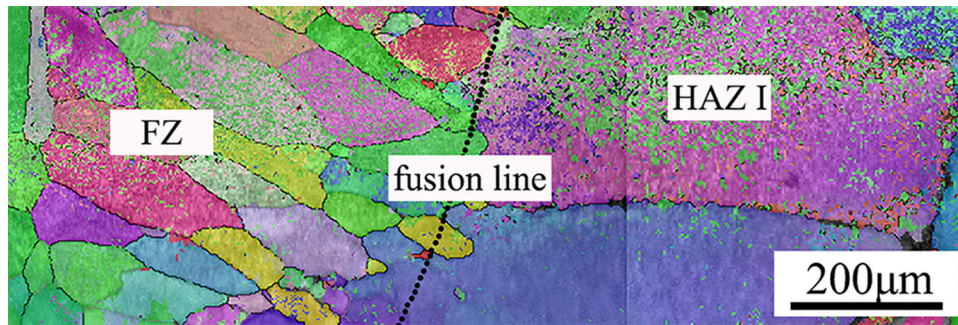
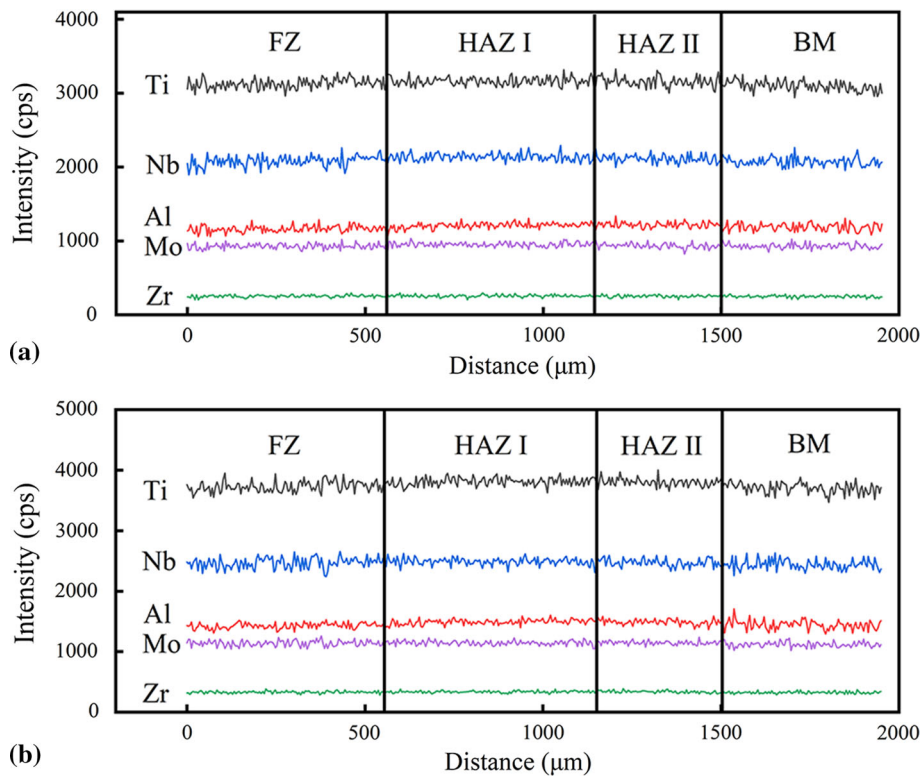


Fig. 7 Microstructure of a welded joint after 810 °C/2 h/AC annealing treatment: (a) overall view, (b) FZ, (c) HAZ I, (d) HAZ II, (e) BM. The red solid line denotes the path for EDS line scanning (Color figure online)



**Fig. 8** EBSD inverse pole figure of the as-annealed joint



**Fig. 9** Element distribution in the (a) as-welded joint and (b) 810 °C/2 h/AC annealed joint

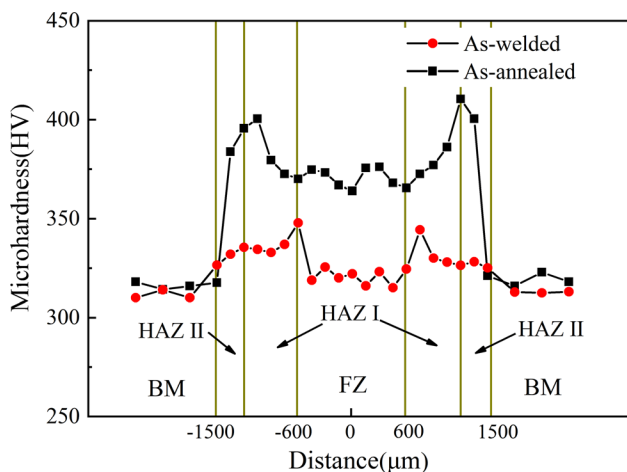


**Fig. 10** Microhardness distribution in the welded joints

enough time to homogenize. Thus, in the following cooling, numerous nuclei of O phase preferentially formed in the solute-rich regions. With the increasing distance in HAZ I from the FZ, the heat input decreased, and the element distribution was more inhomogeneous because of the shorter elevated temperature holding time. Therefore, finer O phase could precipitate during the annealing process, and a higher hardness resulted. On the other hand, the residual O phase in HAZ II grew into coarse morphology during the annealing process, which weakened the strengthening effect. So, the highest hardness appears at the boundary of HAZ I/II.

### 3.3 Mechanical Properties

The tensile stress–strain curves of the base material, as welded joint and 810 °C/2 h/AC annealed (as-annealed) joint at room temperature (RT) and 650 °C are shown in Fig. 11, with the data of yield strength ( $\sigma_y$ ), ultimate strength ( $\sigma_b$ ) and elongation ( $\delta$ ) listed in Table 2.

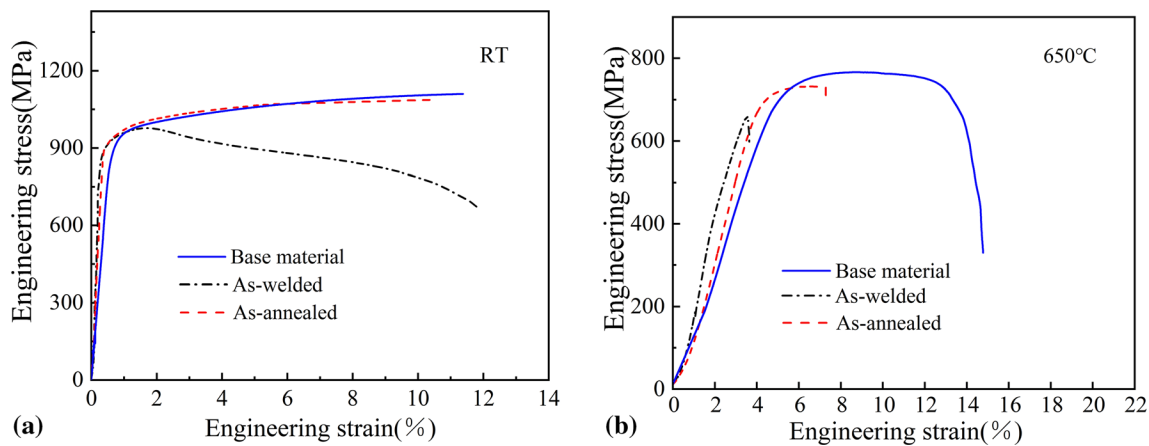


Fig. 11 Tensile stress–strain curves at (a) room temperature and (b) 650 °C

Table 2 Tensile properties at room temperature (RT) and 650 °C

Samples	Temperature	$\sigma_y$ , MPa	$\sigma_b$ , MPa	$\delta$ , %	Fracture location
Base material	RT	925	1093	11.2	...
	650 °C	724	767	14.7	...
As-welded joint	RT	912	979	11.8	FZ/HAZ boundary
	650 °C	660	660	3.4	FZ
As-annealed joint	RT	918	1078	10.3	BM
	650 °C	699	734	7.3	FZ

As shown in Fig. 11(a), one can see that the welded joints exhibit similar  $\sigma_y$  and  $\delta$  to the base material at RT. The as-welded joint even more or less has better  $\delta$  than the base material. But nonuniform deformation (necking) prematurely took place in it (see Fig. 12a), which made the stress decline with deformation, and the ultimate strength is only 91% of the base material. Annealing the welded joint at 810 °C for 2 h promoted the uniform deformation after yielding, and the stress increased with an increasing strain. As a result, a similar ultimate strength to the base material was obtained.

In the tensile test at RT, the as-welded joint fractured at the boundary of FZ/HAZ as shown in Fig. 12(a), as a response to the welding stress and inhomogeneous microstructure. With different thermal histories, the shrinkages within various parts of a joint are inconsistent. On the other hand, the microstructure changes violently across the joint, imparting different parts of the joint with different mechanical performances, as indicated by the changing microhardness. The microhardness reaches the maximum at the boundary of HAZ/FZ. Thus, the strain mismatch and stress concentration were severest there. Correspondingly, cracks initiated and fracture took place along the fusion line. Because the FZ had the lower strength, the plastic deformation was localized in this region, resulting in the necking phenomenon (insert of Fig. 12a).

There is a linear relationship between microhardness and yield stress, which makes the microhardness available to predict the mechanical properties (Ref 27). As shown in Fig. 10, the microhardness was significantly reinforced after the post-weld annealing as a large quantity of fine O phase precipitated in the FZ and HAZ. Consequently, most of the plastic deformation took place in the base material, and the samples also failed in this part (Fig. 12c).

The RT fracture surfaces of both the as-welded and as-annealed joints were composed of ductile dimples, except a few areas with cleavage planes (Fig. 13a and c). Overall, the welded joints failed through ductile fracture. When the tensile test was performed at 650 °C, however, great differences occurred between the samples. As shown in Fig. 11(b), the as-welded joint exhibited almost no ductility and fracture occurred during the elastic deformation stage. In contrast, the annealed joint has a better comprehensive property. The tensile strength reaches 95% of the base material. The ultimate strength is about 734 MPa, and the elongation is still up to 7.3%. As indicated by Fig. 12(b) and (d), both types of the welded joints failed at the FZ at high temperature.

Zhang et al. (Ref 25) performed the tensile test of a laser welded Ti<sub>2</sub>AlNb alloy at 650 °C, it was found that continuous films of O phase would form at the B2/ $\beta$  boundary, due to which cracks formed and propagated along the grain boundary. For the present as-weld joint, the FZ is composed of single B2/ $\beta$  phase. The test temperature of 650 °C is located in the B2/ $\beta$  + O phase region, meaning that the FZ microstructure is unstable at 650 °C. During the heating and holding before the tensile test, O phase nucleated preferentially at the grain boundary of B2/ $\beta$  phase. Consequently, microcracks initiated at the grain boundary of B2/ $\beta$  phase and then quickly propagated as the deformation proceeded, causing a brittle fracture. The fracture surface at 650 °C is significantly different from that at the room temperature, exhibiting the typical feature of intergranular fracture (Fig. 13b). So, the B2/ $\beta$  grain boundary in the FZ is extremely weak at elevated temperature.

After the annealing treatment, the elongation of the welded joint at 650 °C was greatly improved. There are obvious cleavage steps on the fracture surface besides intergranular fracture feature

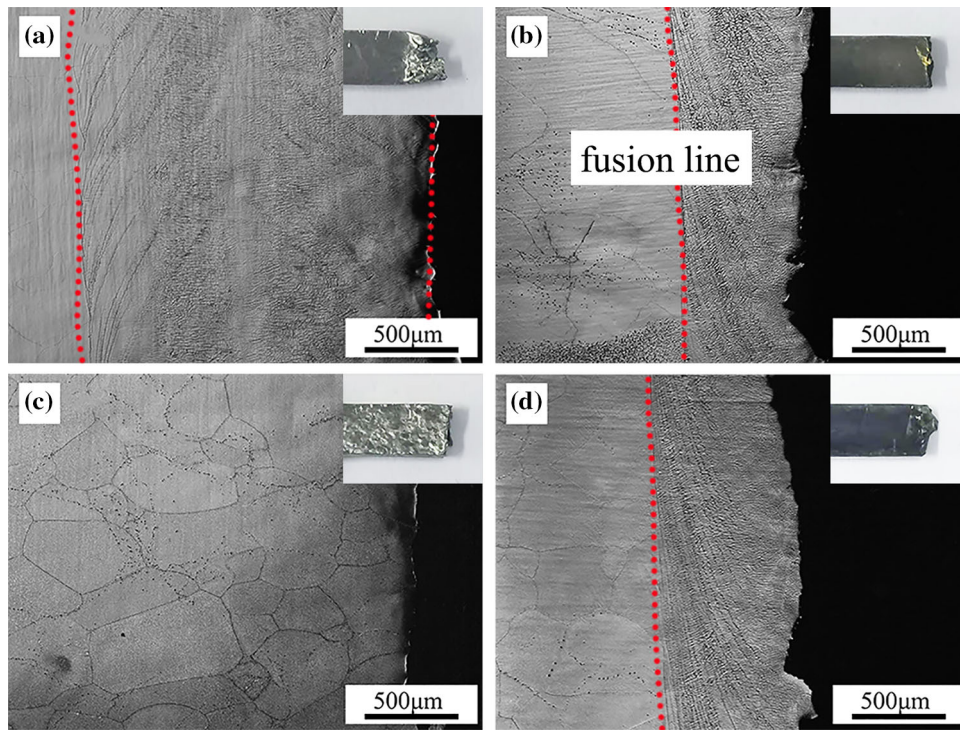


**Fig. 12** The microstructure of longitudinal section near the fracture location of (a, b) as-welded and (c, d) as-annealed joints tested at (a, c) RT and (b, d) 650 °C. The macroscopic images of the fractured sample are inserted

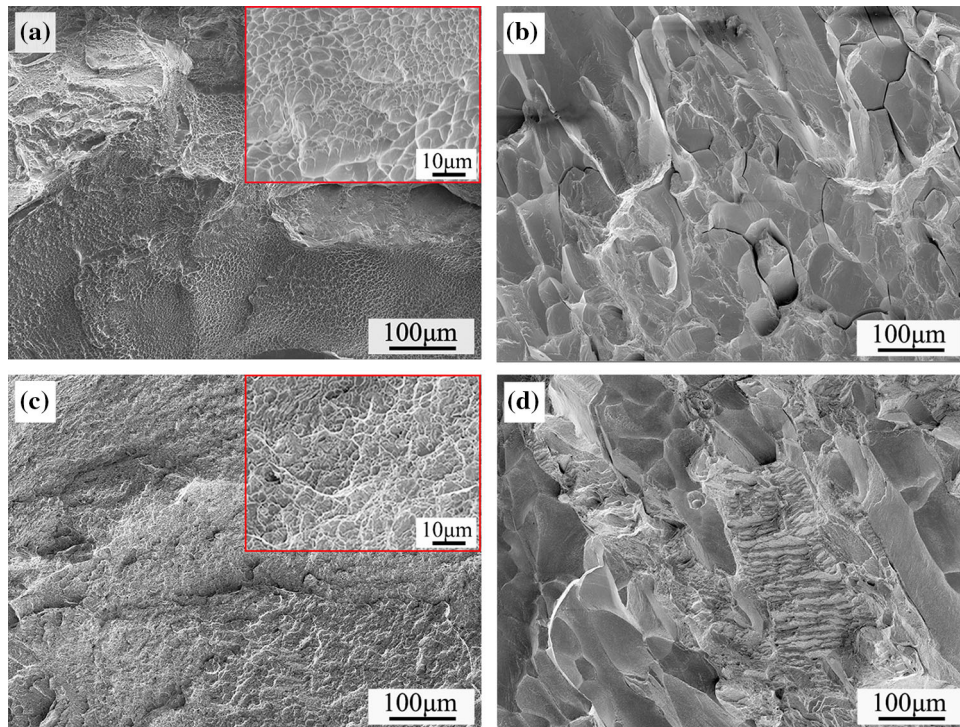


**Fig. 13** Fracture surfaces of (a, b) as-welded and (c, d) as-annealed joints tested at (a, c) RT and (b, d) 650 °C. Inserts are the local magnifications

(Fig. 13d), i.e., the joint exhibits a mixed mode of intergranular and cleavage fractures. The O and B2/ $\beta$  phases that are alternatively distributed have good coordination deformation ability. A slip band can transit from B2/ $\beta$  phase to O phase

without blocking or deflection. The FZ is composed of fine lamellar O phase and B2/ $\beta$  matrix after annealed at 810 °C as shown in Fig. 7(b). Thus, the mechanical performance, especially the elongation, of the welded joint was improved.



## 4. Conclusions

In this paper, a Ti<sub>2</sub>AlNb alloy was electron beam welded, and the microstructure and mechanical property of the welded joints were examined. Conclusions are drawn as follows:

- (1) In an as-welded joint, the FZ is composed of single B2/ $\beta$  phase due to the fast cooling after solidification. The HAZ consists of two parts: HAZ I of B2/ $\beta$  phase and a little residual  $\alpha_2$  phase near the fusion line and HAZ II of B2/ $\beta$ ,  $\alpha_2$  and coarse O phases near the base material. The highest microhardness occurs at the boundary of FZ/HAZ (fusion line), away from which the microhardness decreases gradually.
- (2) When the as-welded joint is subjected to tensile test at RT, the material within the FZ first yield and the plastic strain is highly localized, due to which the stress continuously decreases thereafter. The as-welded joint prematurely breaks without obvious plasticity when it is undergoing the tensile test at 650 °C.
- (3) Post-weld annealing of the welded joint at 810 °C for 2 h can significantly improve the mechanical properties due to precipitation of very fine O phase from the B2/ $\beta$  matrix. As a result, the microhardness in the FZ and HAZ significantly increases. In this case, the as-annealed joint basically exhibits the same mechanical property as the base material at room temperature, with the uniform deformation recovered. The elongation of the as-annealed joints can also reach 7.3% and the ultimate strength is still up to 734 MPa at elevated temperature.

## Acknowledgments

This work was supported by the Science and Technology Special Project of China (K19208) and the National Science and Technology Major Project of China (2017-VI-0004-0075).

## References

1. D. Banerjee, A.K. Gogia, T.K. Nandi and V.A. Joshi, A New Ordered Orthorhombic Phase in a Ti3Al-Nb Alloy, *Acta Metall.*, 1988, **368**, p 71–882.
2. Z.L. Lei, Z.J. Dong, Y.B. Chen, L. Huang and R.C. Zhu, Microstructure and Mechanical Properties of Laser Welded Ti-22Al-27Nb/TC4 Dissimilar Alloys, *Mater. Sci. Eng. A*, 2013, **559**, p 909–916.
3. X. Zhang, H. Li, M. Zhan, Z. Zheng, J. Gao and G. Shao, Electron Force-Induced Dislocations Annihilation and Regeneration of a Superalloy through Electrical In-Situ Transmission Electron Microscopy Observations, *J. Mater. Sci. Technol.*, 2020, **36**, p 79–86.
4. V.A. Esin, R. Mallick, M. Dadé, B. Denand and P. Sallot, Combined Synchrotron x-ray Diffraction, Dilatometry and Electrical Resistivity In Situ Study of Phase Transformations in a Ti<sub>2</sub>AlNb Alloy, *Mater. Charact.*, 2020, **169**, p 1110654.
5. Y. Huang, Y. Liu, Y. Zhang and H. Liang, Thermal Stability and Mechanical Properties of Ti-22Al-25Nb Alloy with Different Initial Microstructures, *J. Alloys. Compd.*, 2020, **842**, p 155794.
6. Y.Q. Fu and Z.S. Cui, Effects of Plastic Deformation and Aging Treatment on Phase Precipitation in Ti<sub>2</sub>AlNb Alloy, *J. Mater. Eng. Perform.*, 2021, **31**(4), p 2633–2643.
7. H. Zhang, N. Yan, H. Liang and Y. Liu, Phase Transformation and Microstructure Control of Ti<sub>2</sub>AlNb-Based Alloys: a Review, *J. Mater. Sci. Technol.*, 2021, **80**, p 203–216.
8. K. Goyal and N. Sardana, Phase Stability and Microstructural Evolution of Ti<sub>2</sub>AlNb Alloys—a Review, *Mater. Today: Proc.*, 2021, **41**, p 951–968.
9. W. Dang, J.S. Li, T.B. Zhang and H.C. Kou, Microstructure and Phase Transformation in Ti-22Al-(27-x)Nb-xZr Alloys During Continuous Heating, *J. Mater. Eng. Perform.*, 2015, **24**(10), p 3951–3957.
10. J. Kumpfert, Intermetallic Alloys Based on Orthorhombic Titanium Aluminide, *Adv. Eng. Mater.*, 2001, **11**, p 851–864.
11. K. Goyal and N. Sardana, Mechanical Properties of the Ti<sub>2</sub>AlNb Intermetallic: a Review, *Trans. Indian Inst. Met.*, 2021, **74**, p 1839–1853.
12. W. Chen, B. Lu and J.W. Li, Development of Ti<sub>2</sub>AlNb Alloys: Opportunities and Challenges, *Adv. Mater. Process*, 2014, **172**, p 23–27.
13. Y. Chu, J. Li, L. Zhu, B. Tang and H. Kou, Characterization of the interfacial-microstructure evolution and void shrinkage of Ti-22Al-25Nb orthorhombic alloy with different surface roughness during diffusion bonding, *Intermetallics*, 2017, **90**, p 119–127.
14. Y. Wang, X.Q. Cai, Z.W. Yang, D.P. Wang, X.G. Liu and Y.C. Liu, Diffusion Bonding of Ti<sub>2</sub>AlNb Alloy Using Pure Ti foil as an Interlayer, *J. Alloy. Compd.*, 2018, **756**, p 163–174.
15. L. Shao, S. Wu and A. Datye, Microstructure and Mechanical Properties of Ultrasonic Pulse Frequency Tungsten Inert Gas Welded Ti-22Al-25Nb (at.%) alloy Butt Joint, *J. Mater. Process. Technol.*, 2018, **259**, p 416–423.
16. X. Chen, F.Q. Xie, T.J. Ma, W.Y. Li and X.Q. Wu, Microstructure Evolution and Mechanical Properties of Linear Friction Welded Ti<sub>2</sub>AlNb Alloy, *J. Alloy. Compd.*, 2015, **646**, p 490–496.
17. X. Chen, F.Q. Xie, T.J. Ma, W.Y. Li and X.Q. Wu, Microstructural Evolution and Mechanical Properties of Linear Friction Welded Ti<sub>2</sub>AlNb Joint During Solution and Aging Treatment, *Mater. Sci. Eng. A*, 2016, **668**, p 125–136.
18. Z. Lei, Z. Dong, Y. Chen, J. Zhang and R. Zhu, Microstructure and Tensile Properties of Laser Beam Welded Ti-22Al-27Nb Alloys, *Mater. Des.*, 2013, **46**, p 151–156.
19. K. Zhang, L. Ni, Z. Lei, Y. Chen and X. Hu, In Situ Investigation of the Tensile Deformation of Laser Welded Ti<sub>2</sub>AlNb Joints, *Mater. Charact.*, 2017, **123**, p 51–57.
20. Z. Lei, K. Zhang, H. Zhou, L. Ni and Y. Chen, A Comparative Study of Microstructure and Tensile Properties of Ti<sub>2</sub>AlNb Joints Prepared by Laser Welding and Laser-Additive Welding with the Addition of Filler Powder, *J. Mater. Process. Tech.*, 2018, **255**, p 477–487.
21. K. Zhang, Z. Lei, L. Ni, H. Zhou and Y. Chen, Improvement in Microstructure and High-Temperature Brittleness of Laser-Welded Ti-22Al-25Nb Joints with the Addition of TiB<sub>2</sub> Powder, *J. Mater. Process. Technol.*, 2021, **288**, p 116848.
22. S. Wang, J. Liu and D. Chen, Tensile and Fatigue Properties of Electron Beam Welded Dissimilar Joints Between Ti-6Al-4V and BT9 Titanium Alloys, *Mater. Sci. Eng. A*, 2013, **584**, p 47–56.
23. J. Sabol, T. Pasang, W.Z. Misiolok and J.C. Williams, Localized Tensile Strain Distribution and Metallurgy of Electron Beam Welded Ti-5Al-5V-5Mo-3Cr Titanium Alloys, *J. Mater. Process. Technol.*, 2012, **212**, p 2380–2385.
24. W. Chen, Z.Y. Chen, C.C. Wu, J.W. Li, Z.Y. Tang and Q.J. Wang, The Effect of Annealing on microstructure and Tensile Properties of Ti-22Al-25Nb Electron Beam Weld Joint, *Intermetallics*, 2016, **75**, p 8–14.
25. C.J. Boehlert, B.S. Majumdar, V. Seetharaman and D.B. Miracle, Part I. The Microstructural Evolution in Ti-Al-Nb O+Bcc Orthorhombic Alloys, *Metall. Mater. Trans. A*, 1999, **30**, p 2305–2323.
26. Z. Bu, Y. Zhang, L. Yang, J. Kang and J. Li, Effect of Cooling Rate on Phase Transformation in Ti<sub>2</sub>AlNb Alloy, *J. Alloys. Compd.*, 2022, **893**, p 162364.
27. G. Liu, Z. Wang, T. Fu and Y. Li, Study on the Microstructure, Phase Transition and Hardness for the TiAl-Nb Alloy Design During Directional Solidification, *J. Alloys. Compd.*, 2015, **650**, p 45–52.

**Publisher's Note** Springer Nature remains neutral with regard to jurisdictional claims in published maps and institutional affiliations.